



HAL
open science

Spatial frequency modulated imaging in coherent anti-Stokes Raman microscopy

Sandro Heuke, Siddharth Sivankutty, Camille Scotté, Patrick Stockton,
Randy Bartels, Anne Sentenac, Hervé Rigneault

► **To cite this version:**

Sandro Heuke, Siddharth Sivankutty, Camille Scotté, Patrick Stockton, Randy Bartels, et al.. Spatial frequency modulated imaging in coherent anti-Stokes Raman microscopy. *Optica*, 2020, 7 (5), pp.417. 10.1364/OPTICA.386526 . hal-02559999

HAL Id: hal-02559999

<https://hal.science/hal-02559999v1>

Submitted on 1 May 2020

HAL is a multi-disciplinary open access archive for the deposit and dissemination of scientific research documents, whether they are published or not. The documents may come from teaching and research institutions in France or abroad, or from public or private research centers.

L'archive ouverte pluridisciplinaire **HAL**, est destinée au dépôt et à la diffusion de documents scientifiques de niveau recherche, publiés ou non, émanant des établissements d'enseignement et de recherche français ou étrangers, des laboratoires publics ou privés.



Spatial frequency modulated imaging in coherent anti-Stokes Raman microscopy

SANDRO HEUKE,¹ SIDDHARTH SIVANKUTTY,¹ CAMILLE SCOTTE,¹ PATRICK STOCKTON,² RANDY A. BARTELS,² ANNE SENTENAC,¹ AND HERVÉ RIGNEAULT^{1,*}

¹Aix Marseille Univ, CNRS, Centrale Marseille, Institut Fresnel, Marseille, France

²School of Biomedical Engineering, Colorado State University, Fort Collins, Colorado 80523, USA

*Corresponding author: herve.rigneault@fresnel.fr

Received 23 December 2019; revised 7 February 2020; accepted 2 March 2020 (Doc. ID 386526); published 1 May 2020

For sparse samples or in the presence of ambient light, the signal-to-noise ratio (SNR) performance of single-point-scanning coherent anti-Stokes Raman scattering (CARS) images is not optimized. As an improvement, we propose replacing the conventional CARS focus-point illumination with a periodically structured focus line while continuing to collect the transmitted CARS intensity on a single detector. The object information along the illuminated line is obtained by numerically processing the CARS signal recorded for various periods of the structured focus line. We demonstrate experimentally the feasibility of this spatial frequency modulated imaging (SPIFI) in CARS (SPIFI-CARS) and SHG (SPIFI-SHG) and identify situations where its SNR is better than that of the single-point-scanning approach. © 2020 Optical Society of America under the terms of the OSA Open Access Publishing Agreement

<https://doi.org/10.1364/OPTICA.386526>

1. INTRODUCTION

Coherent anti-Stokes Raman scattering (CARS) microscopy has shown great utility for all kinds of biomedical [1] and material science investigations [2,3]. Yet, the expected integration of CARS microscopes into the standard equipment of biolabs, hospitals, or quality control of industrial products has not been achieved. To advance towards routine applications, the utility of a technique has to outweigh its costs. Thus, the value of the label-free contrast provided in CARS microscopy together with the image acquisition rate at a given signal-to-noise ratio (SNR) level has to outweigh the price of the equipment as well as its maintenance. Since CARS laser systems have benefited from recent advances in high-power fiber laser technology resulting in maintenance-free, co-propagating two-color laser systems [4–6], the remaining task to accomplish is the acceleration of data collection.

Since its first implementations in imaging [7,8], state-of-the-art CARS microscopy has been performed by single-focus laser scanning microscopy (LSM) limiting the SNR required for high scanning speeds, as permanent damage of biological tissue is frequently observed above 50 mW [with standard ps-laser systems at 80 MHz repetition rate and excitation numerical apertures (NAs) larger than 0.5]. To increase the scanning speed and SNR, while limiting the damage of the sample, it was proposed to exploit the power potential of novel fiber laser sources using simultaneous illumination of several points, either by multi-focus [9,10] approaches or by wide-field implementations [11,12]. The former suffers from either forward scattering inherent to CARS radiation [9] or a

complex experimental implementation [10]. Theoretically, wide-field CARS outperforms all other approaches in terms of signal acquisition speed for thin samples, possibly allowing large fields of view [13], but its image fidelity suffers for bulk samples from linear scattering, absorption, and phase-matching considerations.

Here, we present an alternative positioned multiplex-CARS scheme using the interference of various focused line illumination patterns and a single element detector [photomultiplier tube (PMT)] to obtain a 1D CARS profile. Lateral scanning of the line focus results in 2D CARS images. We use here the concept of spatial frequency modulated imaging (SPIFI) [14,15], which has been recently applied to incoherent linear Raman imaging [16], and extend it to CARS microscopy. The pump and Stokes beam are formed separately into light-sheets and directed towards the sample. Using a rotating amplitude mask [14], the Stokes beam is spatially modulated in time while the generated anti-Stokes radiation is detected by a single element detector (PMT). Fourier transforming the time trace of the CARS signal yields the desired sample 1D profile.

There are several advantages connected to this approach: (1) Since the laser power is distributed along a line, the total excitation power can be increased, yielding more CARS photons than any point-focus approach could generate assuming the same power density. As a result, the imaging rate can be greatly enhanced. (2) The bucket single-element detector greatly improves the tolerance towards scattering or aberrations by simply collecting the CARS generated photons. (3) As an advantage over wide-field techniques, SPIFI-CARS retains the intrinsic confocality and, therefore, the ability for 3D sectioning. (4) The proposed implementation

differs from a standard CARS laser scanning microscope only by adding a rotating mask in combination with a cylindrical lens. Thus, compared to a multi-focus approach, the required extension for SPIFI-CARS is inexpensive and simple. (5) SPIFI-CARS requires scanning of the sample in only one direction, which avoids difficulties found in stitching 2D-LSM images [17,18].

First, we present a simple analytical model to establish the relation between the SPIFI-CARS time trace and the sample. We find that performing a simple Fourier transform of the CARS signal time trace yields the spatial distribution of the CARS scatterers similar to what has been reported for coherent SPIFI analysis [19] and implementation [20]. Second, we present an experimental implementation that allows imaging of 100 lines per second with a lateral width of about 100 μm [full width at half maximum (FWHM)]. For demonstration, we show and discuss SPIFI-CARS images of polymer and biological samples. Finally, a fully vectorial model for numerical calculations is presented and applied to evaluate the performances of SPIFI-CARS versus LSM-CARS for different noise models and sample structures.

2. ANALYTICAL FRAMEWORK

While the image formation of isotropically radiating emitters in incoherent SPIFI is well understood [14,15], the modeling of coherent SPIFI-CARS imaging is yet to be done. In this section, we briefly describe its principle under a simplifying hypothesis, a full modeling being provided in Section 5.

We consider an optical microscope, functioning in transmission with the optical axis directed along the z direction. The sample is illuminated by two x -polarized pump and Stokes beams, $E_{p,x}$ and $E_{s,x}$, respectively, and all the x -polarized CARS radiation is collected at the image plane by a single-element detector. We assume that only the χ_{1111} component of the nonlinear anti-Stokes susceptibility tensor of the sample $\chi_{\text{aS}}^{(3)}$ is involved in the generation of the CARS radiation. For simplicity, the sample is assumed to be infinitely thin along the z and y directions, which is, in practice, related to a spatial average of the CARS signal across the thickness of the line focus that serves as an effective 1D spatial profile. Further, the sample is placed at the object focal plane corresponding to $z = 0$, so that $\chi_{\text{aS}}^{(3)}$ reads

$$\overset{\leftrightarrow}{\chi}_{\text{aS}}^{(3)} = \chi_{\text{aS}}^{(3)}(x)\delta(y)\delta(z), \quad (1)$$

where $\chi_{\text{aS}}^{(3)}$ is proportional to the vibrational scatterer density $N(x)$ that provides information about the concentration of the targeted molecular groups. $\delta(m)$ denotes the 1D Dirac delta function along the axis m . In our configuration, the pump beam propagates along the optical axis, so that E_p is constant at the object focal plane while the Stokes beam is periodically modulated by a rotating mask, and its expression at $y = z = 0$ reads

$$E_{s,x}(k_m, x) \propto \frac{1}{2}[1 + \cos(k_m x)], \quad (2)$$

where $k_m = 2\pi\kappa t$ is the time-dependent spatial k -vector of the Stokes intensity modulation. $\kappa = \Delta k v_r$ is the chirp parameter relating the lateral position on the modulation mask to the modulation frequency [21]. The grating parameter Δk [unit 1/m] defines the amplitude profile in transmission of the rotating disk, while v_r is the angular velocity [unit rad/s] [16].

For illustration, Eq. (2) is modeled in the inset of Fig. 1.

Under these illumination conditions, the effective source of anti-Stokes radiation is given by the anti-Stokes polarization:

$$\begin{aligned} \mathbf{P}_{\text{aS}}^{(3)}(\mathbf{r}) &= \overset{\leftrightarrow}{\chi}_{\text{aS}}^{(3)}(\mathbf{r})\mathbf{E}_p^2(\mathbf{r})\mathbf{E}_s^*(\mathbf{r}), \\ \mathbf{P}_{\text{aS}}^{(3)}(x, y, z) &= \chi_{\text{aS}}^{(3)}(x)E_{p,x}^2 E_{s,x}^*(k_m, x)\delta(y)\delta(z)\hat{\mathbf{x}}. \end{aligned} \quad (3)$$

In SPIFI-CARS, the radiated anti-Stokes intensity collected by the objective of the microscope is detected on a single-element detector. A temporal signal, $I_{\text{aS}}(k_m)$, is then obtained, recalling that $k_m = 2\pi\kappa t$ is the modulation frequency of the periodic Stokes illumination along the x axis. In this section, we consider the anti-Stokes radiation to be collected by a perfect imaging system detecting all the photons radiated by the sample. Further, we neglect all phase and phase-matching terms but inherently assume equal efficiency of signal generation for all kinds of sample structures (note that the sample's 1D structure within this model as well as the intrinsic confocality of the real light-sheet CARS experiment greatly relax phase matching). Thus, the detected intensity is assumed to be proportional to the integral of the source intensity:

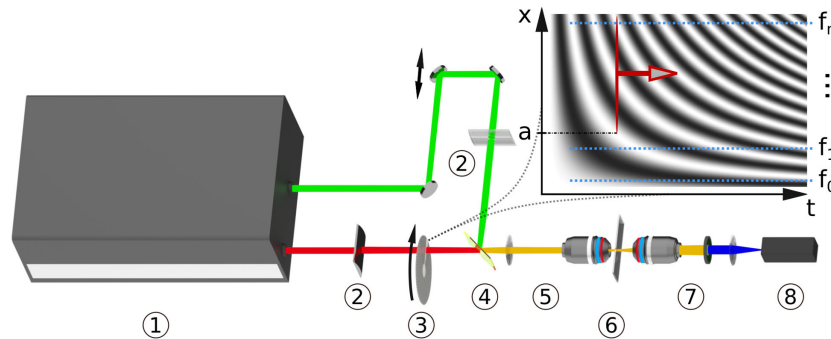


Fig. 1. Experimental setup: (1) tunable dual-color fs laser, (2) cylindrical lens, (3) rotating disk with imprinted modulation pattern, (4) dichroic beam combiner, (5) 4f-system 20x, (6) sample, (7) condenser lens and dielectric filter, and (8) analog PMT. Inset: the graph shows the modulation pattern printed circularly around the rotating disk. The linear modulation chirp of the Stokes light-sheet leads to different modulation frequencies at different x -lateral sample positions with $f_0 < f_1 < \dots < f_n$.

$$\begin{aligned}
I_{aS}(k_m) &\propto \int_{-\infty}^{\infty} |\mathbf{P}_{aS}^{(3)}(\mathbf{r})|^2 d\mathbf{r}, \\
I_{aS}(k_m) &\propto \int_{-\infty}^{\infty} |\chi_{aS}^{(3)}|^2(x) [1 + \cos(k_mx)]^2 dx, \\
I_{aS}(k_m) &\propto \int_{-\infty}^{\infty} |\chi_{aS}^{(3)}|^2(x) \left(\frac{3}{2} + 2 \cos(k_mx) + \frac{1}{2} \cos(2k_mx) \right) dx, \\
I_{aS}(k_m) &\propto \frac{3}{2} \langle |\chi_{aS}^{(3)}|^2 \rangle + \text{Re} \left(2\mathcal{F} \left[|\chi_{aS}^{(3)}|^2 \right] (k_m) \right. \\
&\quad \left. + \frac{1}{2} \mathcal{F} \left[|\chi_{aS}^{(3)}|^2 \right] (2k_m) \right), \tag{4}
\end{aligned}$$

where $\mathcal{F}[f]$ is the Fourier transform of f defined by $\mathcal{F}[f](k) = \int f(x) e^{ikx} dx$. As the result of Eq. (4), the detected photons can be separated into three contributions: the first term is constant for all modulation patterns and linked to the spatial average over the line of the sample density. It does not provide any spatial information but contributes to the shot noise. We will show and discuss simulations in a following section to outline a situation where such an offset is considered a drawback. The second and third terms of Eq. (4) contain signal that varies with time, bearing spatial information of the sample.

To distinguish the three terms of Eq. (4), the excitation beam and sample are not placed at the center but at the radial position a of the modulation disk (see also Fig. 2). Alternatively, we could have defined $E_{S,x}(x) = 1 + \cos(k_mx - \omega_a t) = 1 + \cos[k_m(x - a)]$, where $\omega_a = 2\pi\kappa a$ is the carrier angular frequency of the rotating disk. In both cases, the detected signal reads

$$\begin{aligned}
I_{aS}(k_m) &\propto \frac{3}{2} \langle |\chi_{aS}^{(3)}|^2 \rangle \delta(x) + \text{Re} \left(2\mathcal{F} \left[|\chi_{aS}^{(3)}|^2 \right] (k_m) e^{ik_ma} \right. \\
&\quad \left. + \frac{1}{2} \mathcal{F} \left[|\chi_{aS}^{(3)}|^2 \right] (2k_m) e^{2ik_ma} \right). \tag{5}
\end{aligned}$$

Performing an inverse Fourier transform with respect to k_m of the whole temporal signal yields

$$\begin{aligned}
\mathcal{F}^{-1}[I_{aS}](x) &= \frac{1}{2\pi} \int I_{aS}(k_m) \exp(-ik_mx) dk_m \\
&\propto \frac{3}{2} \langle |\chi_{aS}^{(3)}|^2 \rangle \delta(x) + |\chi_{aS}^{(3)}|^2(x - a) \\
&\quad + |\chi_{aS}^{(3)}|^2(-x + a) + \frac{1}{4} |\chi_{aS}^{(3)}|^2(x/2 - a) \\
&\quad + \frac{1}{4} |\chi_{aS}^{(3)}|^2(-x/2 + a). \tag{6}
\end{aligned}$$

Expression (6) shows that for a big enough (bigger than the sample or the illumination beam width), the overlap between the different contributions can be minimized, and the square modulus of the sample third-order susceptibility tensor can be recovered (see Fig. 2). The same reasoning can be conducted using a periodically structured pump and a uniform Stokes beam. This option yields additional “echos,” such as $|\chi_{aS}^{(3)}|^2(x/3 - a)$, $|\chi_{aS}^{(3)}|^2(x/4 - a)$ [22].

3. EXPERIMENTAL IMPLEMENTATION

The experimental setup is presented schematically in Fig. 1. A tunable multi-color fs-laser system (Coherent, Chameleon Discovery) provides two synchronized output beams. The Stokes beam (1040 nm, 160 fs) is focused to a line on the modulator disk using a 100 mm focal length cylindrical lens (Thorlabs, LJ1567RM-B). The modulator disk features the grating constant $\Delta k = 35 \text{ mm}^{-1}$. For manufacturing reasons, the pattern used experimentally is described by $1/2 + \text{sgn}[\cos(k_mx + \omega_a t)]/2$ [and not by Eq. (2)]. For conciseness, the impact of higher-order refractions was neglected, and we recommend reference [21] for further details. The disk is mounted onto a stepper motor (MCL-3006, Faulhaber) and rotated at a 100 Hz velocity. The pump beam (660–1320 nm, 100 fs) is shaped separately into a light-sheet by a second cylindrical lens (Thorlabs, LJ1695RM-B). Both beams are combined via a dichroic beam splitter (Semrock, Di02-R980) and temporally superimposed using a delay stage. The joint light-sheets are focused (Nikon, CFI PLAN APO LBDA 20X, NA: 0.75) onto the sample using a 4f-system with 20x magnification (see also Fig. 2). The power at the sample does not exceed 250 mW per color in total across the line illumination’s excitation profile. For image generation, the position of the line focus is kept static, while the sample is moved in 2D using translational stages (PI, M-110.12S) (see Figs. 3(a) and 3(b) for the scanning scheme). The CARS radiation is collected in forward direction using a low-NA objective lens (Olympus, RMS10X, NA: 0.25). Dielectric filters (Semrock FF01-775/SP, FF01-643/20 for CARS, Semrock FF01-525/39-25 for SHG) are used to block the excitation beams. The transmitted CARS or SHG signal is detected with an analog photo-electron-multiplier tube (PMT, Hamamatsu, R9110). The voltage output of the PMT is direct-current blocked (Thorlabs, EF500), low-pass filtered at $f \leq 100 \text{ kHz}$ (Thorlabs, EF502), and digitized at 0.5 MHz clock rate by a data acquisition card (DAQ, NI USB-6361). The control of the setup as well as data processing is performed using MATLAB (R2018b).

4. EXPERIMENTAL RESULTS

To obtain the CARS profile of a single 1D line, the structured disk has to perform one complete rotation, while the PMT is read out continuously. An example of such a time trace is displayed in blue in Fig. 4 for a homogeneous sample (olive oil).

The CARS signature is found by zooming into the relevant frequency area of the Fourier transform (see also Fig. 2). From Fig. 4, our setup can achieve a frequency to space encoding with a FWHM of approximately 80 μm . Restricting the following image acquisition to pixels within the FWHM yields 40 separate pixels and, therefore, an x resolution of 2 μm along the active line, while the y resolution remains diffraction limited at around 500 nm. The difference of a factor of approximately four arises as the Stokes and the pump beam determine independently the resolution in x and y directions. A more rigorous derivation of the non-isotropic lateral resolution can be found in Ref. [21] Section 6. Here, the resolution defined by the pump exceeds the one of the Stokes due to the shorter wavelength of the pump as well as its nonlinearity in signal generation, as evident from Eq. (3).

As outlined in Fig. 3(b), SPIFI-CARS images are obtained by moving the sample continuously perpendicular (blue box) to the long axis of the line focus (red line). Several scans are stitched to obtain larger images using the Image Composite Editor (ICE

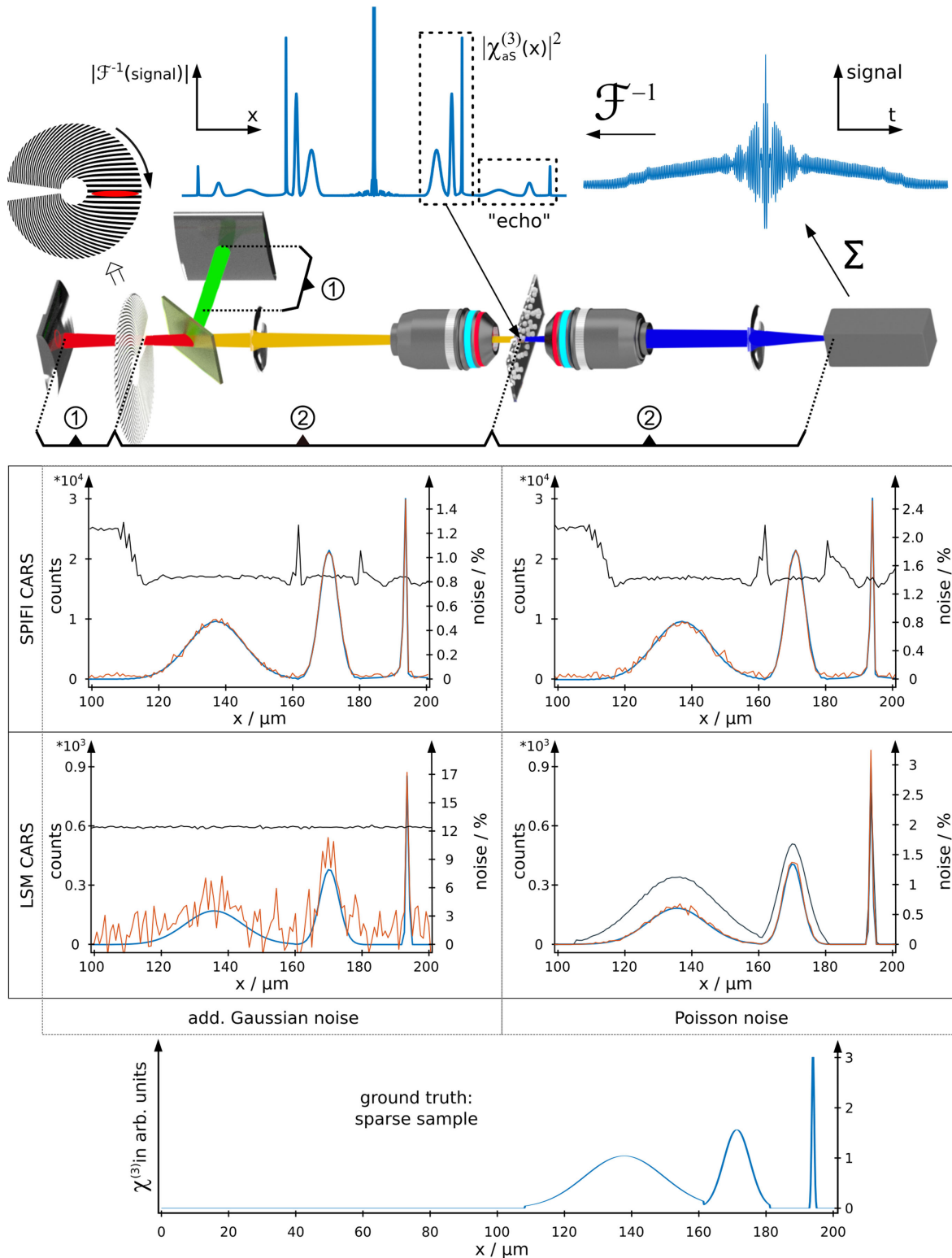


Fig. 2. Comparison of SPIFI and laser scanning microscopy (LSM) CARS imaging on synthetic data. In SPIFI-CARS, the excitation fields are focused along a line (x axis) due to cylindrical lens, and the Stokes beam is periodically structured by a rotating mask: step ①. In LSM-CARS, the excitation fields are point-focused. In both cases, the anti-Stokes radiation detected by the collection objective is sent towards a unique detector. In SPIFI-CARS, the time-dependent signal corresponds to different periods of the structured Stokes fields, while in LSM-CARS, it corresponds to different positions of the sample, which is translated along the x axis: step ②. In SPIFI CARS, the signal is Fourier transformed to recover the sample profile along x , while in LSM-CARS, the detected intensity is related directly to the sample. We study the impact of noise on the SPIFI and LSM profiles when the signals are deteriorated with the same additive Gaussian noise or with a Poisson noise obtained with the same excitation peak power densities. The blue lines correspond to the recovered profiles for noiseless signals. The orange curves correspond to the recovered profiles for noisy signals. The black lines show the relative error $\text{Err}(x) = \frac{1}{N} \sum_{\text{noise}=1}^N |f_{\text{true}}(x) - f_{\text{noise}}(x)| / f_{\text{max}}$, where $f_{\text{noise}}(x)$ is the reconstructed profile for a given noise realization.

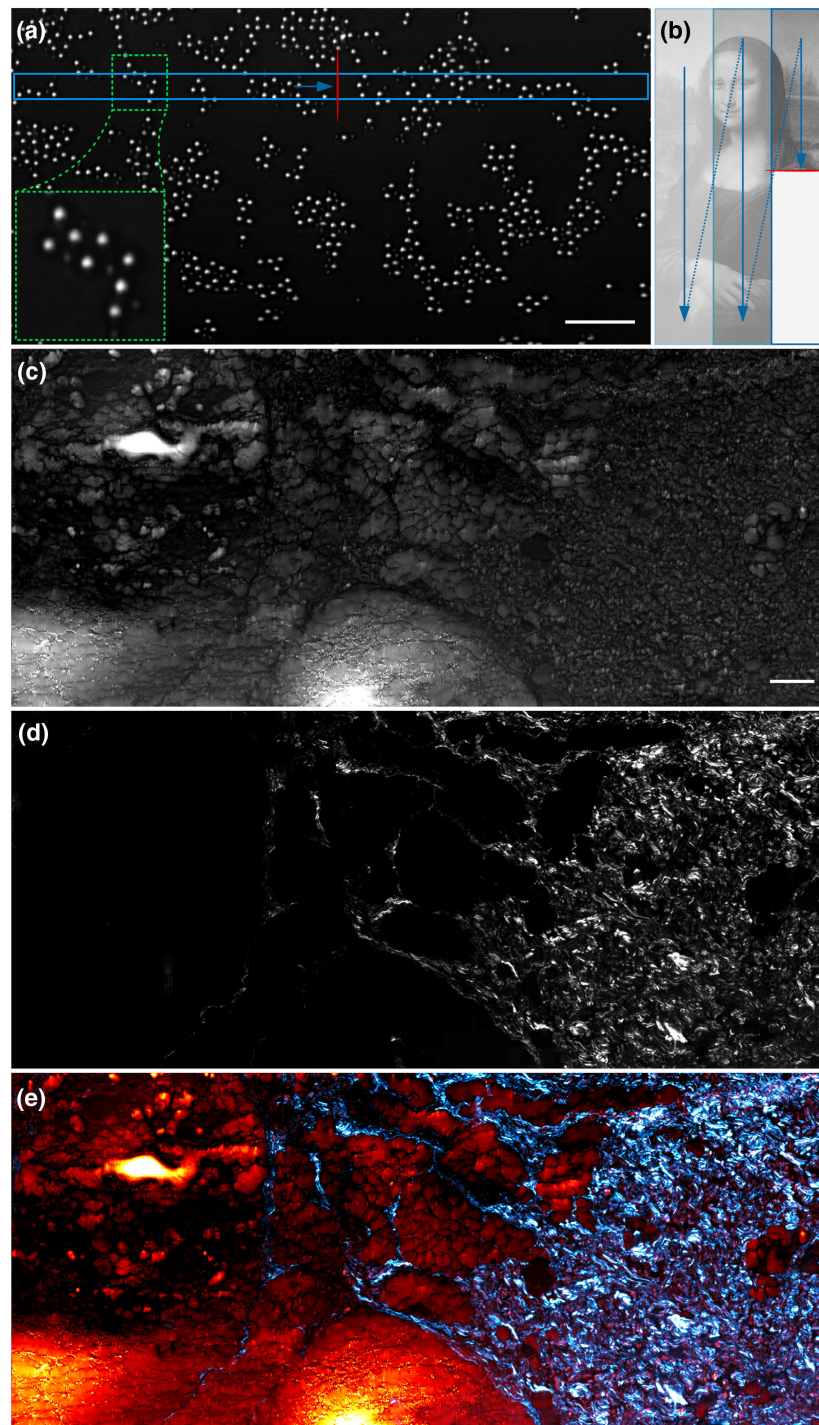


Fig. 3. SPIFI-CARS imaging: (a) SPIFI-CARS image of a mixture of 30 μm polystyrene (PS) and 20 μm poly(methyl methacrylate) (PMMA) beads acquired at 3050 cm^{-1} . (b) Image scanning scheme rotated by 90° . (c) SPIFI-CARS image of a 20 μm thick human breast tissue section. (d) SPIFI-SHG image of the same section. (e) Composite SPIFI-CARS/SHG image. Scale bar: 200 μm . Line focus scanning direction: from left to right.

2.0.3, Microsoft) [23]. For displaying purposes, the data of two full disk rotations were averaged for the reconstruction of a line profile.

Figure 3(a) displays a SPIFI-CARS image of a mixture of 30 μm polystyrene and 20 μm poly(methyl methacrylate) (PMMA) beads imaged at a Raman shift of 3050 cm^{-1} . As a second example, the transition from connective to adipose tissue of a human breast tissue section of 20 μm thickness was obtained at 2850 cm^{-1} (SPIFI-CARS) followed by a SPIFI-SHG image acquisition [22]

to reveal the localization of collagen fibers. We refer to Ref. [24] for comparison to an LSM-CARS image of a human adipose tissue section. The total image acquisition time for each image composed of 20 vertical lines of the sample amounts to 10 min. Since at minimum one rotation of the spinning disk is required to retrieve a single line profile, the current speed limitation of our setup is set by the motor-disk combination with a maximum of 6000 rot/min (100 Hz). Assuming 40 pixels per line results in an effective pixel

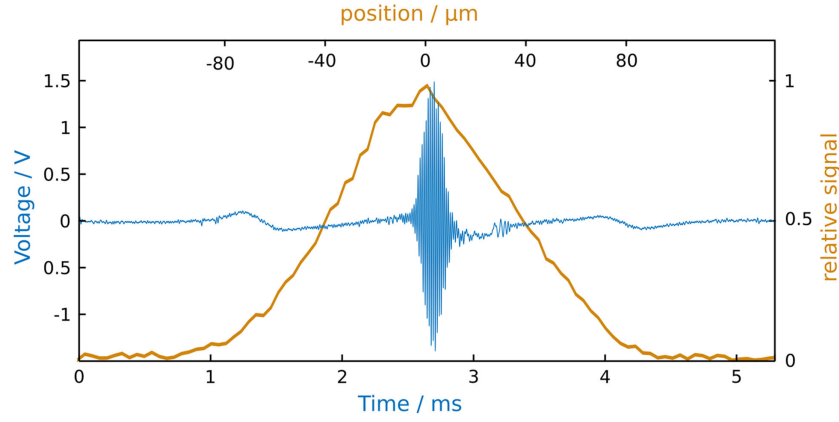


Fig. 4. Time-trace and sample profile: the CARS signal (blue) is collected continuously for each rotation of the modulation pattern. Fourier transforming this time trace after one complete turn yields the profile (orange) of the homogeneous oil sample multiplied by the illumination function.

dwell time of 250 μs (500 μs used for displaying). The latter may be reduced by increasing the number of lines on the spinning disk that are illuminated by the Stokes light sheet, utilizing faster motors or replacing the motor–disk combination by a laser scanning mirror in combination with a reflective modulation pattern [25] or by acousto-optical deflectors (AODs) [26]. Thus, our SPIFI-CARS implementation does not outperform laser scanning approaches in terms of speed but uses power densities that are a factor of 20 lower comparing the 250 mW per color for SPIFI-CARS spread over more than 100 μm (approx. 3.6 mW/ μm^2) with LSM-CARS using standard power levels of 25 mW spread over circles of 700 nm (FWHM) diameter (approx. 65 mW/ μm^2).

5. NUMERICAL IMPLEMENTATION

In this section, we present simulations of SPIFI-CARS images inspired from the model presented in Ref. [13]. The imaging configuration is shown in Fig. 3. We assume that the sample is very thin along the z direction and placed at the object plane of a collection objective that coincides with the image plane of a 4f imaging system with magnification M . At the object focal plane of the latter, a rotating mask is placed modulating the Stokes beam. The Stokes field is focused along the x axis at the mask position $z = Z_{\text{mask}}$ due to a cylindrical lens with numerical aperture given by $\sin \alpha$ (see Fig. 2). The x -polarized Stokes field reads [27]

$$E_{S,x}(x, y, Z_{\text{mask}}^-) = \int_{-\alpha}^{\alpha} \sqrt{\cos \theta} \exp[ik_S(y \sin \theta + Z_{\text{mask}}^- \cos \theta)] d\theta, \quad (7)$$

where k_S is the Stokes angular wavenumber.

Just after the mask plane, the Stokes field is multiplied by the time-dependent modulation pattern:

$$E_{S,x}(x, y, Z_{\text{mask}}^+) = \frac{1}{2} [1 + \cos(k_m x)] E_{S,x}(x, y, Z_{\text{mask}}^-), \quad (8)$$

where we recall that $k_m = \kappa t$. The Stokes field propagates through the 4f imaging system, and its expression at the sample plane is given by Eq. (8) except that the space variables on the left-handed term, (x, y) , are replaced by (Mx, My) to account for the magnification. The pump field is focused along the same line as that of the Stokes beam, but it does not pass through the mask, so that its

expression at the sample plane is given by Eq. (7) with k_S replaced by k_p .

Once the pump and Stokes fields are known at the sample plane, the anti-Stokes polarization is calculated using Eq. (3), and the anti-Stokes field radiated in the far field is obtained from the source's 3D Fourier transform, [13,28]. More precisely, the flux of the Poynting vector per solid angle radiated by the anti-Stokes polarization in the direction $\mathbf{k} = k_{\text{aS}}[\sin \theta \cos \phi \hat{\mathbf{x}} + \sin \theta \sin \phi \hat{\mathbf{y}} + \cos \theta \hat{\mathbf{z}}]$ reads

$$\frac{d\Phi}{d\Omega}(\theta, \phi) = \frac{c k_{\text{aS}}^4}{8\pi} |\tilde{\mathbf{P}}_{\text{aS}}^{(3)}(\mathbf{k}) - \hat{\mathbf{k}} \cdot \tilde{\mathbf{P}}_{\text{aS}}^{(3)}(\mathbf{k}) \hat{\mathbf{k}}|^2, \quad (9)$$

where $\hat{\mathbf{k}} = \mathbf{k}/k_{\text{aS}}$, and $\tilde{\mathbf{P}}_{\text{aS}}^{(3)}(\mathbf{k}) = \int \mathbf{P}_{\text{aS}}^{(3)}(\mathbf{r}) \exp(-i\mathbf{k} \cdot \mathbf{r}) d\mathbf{r}$. In SPIFI, the anti-Stokes radiation that propagates within the solid angle of the collection objective is sent towards a unique detector. Introducing the collection angle $\Theta = \sin^{-1} \text{NA}_{\text{coll}}$ of the collection objective, the power I detected by the bucket detector is

$$I = \int_0^{2\pi} d\phi \int_0^{\Theta} \frac{d\Phi}{d\Omega}(\theta, \phi) \sin \theta d\theta. \quad (10)$$

The CARS time trace $I(t_n)$ is obtained by estimating I for different structured Stokes illuminations with $2\pi k_m = \kappa t_n$ and $t_n = n\Delta t$.

The numerical calculations were performed using a thin rectangular sample with $L_x = 200 \mu\text{m}$, $L_y = 10 \mu\text{m}$, and $L_z = 200 \text{nm}$ (single z layer) whose third-order susceptibility tensor is discretized over a cubic mesh with steps of 200 nm. The sample susceptibility was set constant within y and z directions, while the sample structure in x direction was modeled by three Gaussians with various widths, mimicking polymer rods of different sizes (see Fig. 2). We assumed $M = 1$ (no magnification), $\alpha = 10^\circ$, $\lambda_S = 1030 \text{nm}$, $\lambda_p = 796 \text{nm}$ (2850cm^{-1}), $\Theta = 53^\circ$. The calculations were repeated for 2300 steps in time, corresponding to a full turn of the disk pattern. It yielded a regular sampling of $k_m \in -0.1172 \text{mm}^{-1} + 0.1172 \text{mm}^{-1}$ with steps of 100nm^{-1} , which ensured an accurate frequency probing of the sample. The SPIFI time trace was deteriorated with either Gaussian additive noise or Poisson noises. The latter were obtained by choosing excitation peak power densities so that 10^4 photons were collected for a homogeneous sample with $\chi_{1111}^{(3)} = 1$. The Gaussian white noise

was set to 10 counts on average per time step. Then, a sample profile was recovered by simply performing a 1D inverse fast Fourier transform of the SPIFI-CARS time trace $I(t_n)$.

For comparison, we also simulated the signal that would be obtained with LSM-CARS. In this case, the focal fields were computed as in Ref. [29], and the sample was moved in the x direction to obtain its 1D profile. The signal was deteriorated by the same Gaussian additive noise per time step or Poisson noise obtained with the same excitation peak power densities [W/m^2] and signal integration times per readout as in the SPIFI configuration.

The synthetic results are summarized in Fig. 2. The blue curves represent the noise-free reconstructed profile, while the orange curves outline the sample profile with additive Gaussian or Poisson noise included in the signals. We also introduce the absolute value of the profile mean error Err normalized to the counts of the highest peak defined as $\text{Err}(x) = \frac{1}{N} \sum_{\text{noise}=1}^N |f_{\text{true}}(x) - f_{\text{noise}}(x)| / f_{\text{max}}$, where N is the number of noise realizations, which was set to 5000, and $f_{\text{noise}}(x)$ is the reconstructed profile for a given noise realization.

We observe from Fig. 2 that, in the case of SPIFI-CARS, the shape of $\text{Err}(x)$ is similar for both the additive Gaussian and Poisson noises. This result confirms the remark noted in Section 2. The Poisson noise in SPIFI-CARS is governed by the number of photons stemming from the constant term in Eq. (4), which depends on the average sample density over the line. It remains the same whatever the time step and eventually acts as a Gaussian additive noise. Thus, sparsity of the sample will reduce the off-set photon noise with an estimated break-even point of half the field of view being empty compared to LSM-CARS. On the contrary, for LSM-CARS, $\text{Err}(x)$ is constant for the additive Gaussian noise but follows the CARS intensity for the Poisson noise, i.e., it increases and decreases with the scatterer density. When the Gaussian additive noise is dominant, $\text{Err}(x)$ is about 14 times smaller in the SPIFI-CARS configuration than in the LSM-CARS one. When the Poisson noise is dominant, the SPIFI-CARS relative error is similar to that of LSM-CARS at positions where the scatterer density is high but is bigger than that of LSM-CARS at positions where the scatterer density is low.

6. DISCUSSION

The number of photons detected in SPIFI-CARS being orders of magnitude bigger than that of LSM-CARS, SPIFI-CARS is less sensitive to a Gaussian additive noise (which does not depend on the detected intensity) than LSM-CARS. In particular, we have observed that SPIFI-CARS is weakly affected by ambient light. The experimental results presented in Fig. 3(a) were acquired with the lab's ceiling light switched on. Thus, SPIFI-CARS could be the preferred method if the ambient light sources can not be sufficiently dimmed.

When the photon noise is prevalent, SPIFI-CARS is encumbered by the shot noise stemming from the background CARS radiation of the averaged sample density over the line. We have shown that LSM-CARS may perform better than SPIFI-CARS, in particular when imaging low concentrations in an otherwise dense sample. This configuration is encountered, for example, when using standard PMTs as the detector (low dark noise), in biomedical applications featuring a considerable nonresonant background [3]. In this case, a spatially multiplexed detection version of SPIFI-CARS may be an interesting option, as the splitting

of the anti-Stokes radiation on Q different PMTs would reduce the influence of the background shot noise. Still, SPIFI-CARS is the method of choice for sparse samples, such as isolated adipocytes on a cover slip, due to the vastly increased illumination time and generated signal photons.

Since we are using a femtosecond duration laser pulse, our current implementation has a poor spectral resolution (200 cm^{-1}). This issue can be addressed by switching to spectral focusing [30,31] or to high peak power ps-laser sources. As a rule of thumb, the required power levels of suitable laser sources may be estimated from $P_{\text{SPIFI}}/d_{\text{line}} = P_{\text{LSM}}/d_{\text{focus}}$, where P_{SPIFI} and P_{LSM} are the power levels for the SPIFI approach and conventional LSM techniques, while d_{line} and d_{focus} are the widths along x of the line and point focus, respectively. As an example, for $d_{\text{line}} = 1 \text{ mm}$, $d_{\text{LSM}} = 1 \mu\text{m}$, and $P_{\text{LSM}} = 10 \text{ mW}$ (80 MHz rep. rate), the required output power per color is determined as $P_{\text{SPIFI}} = 10 \text{ W}$. Although, ultrafast lasers with $>5 \text{ W}$ average power are commercially available, the handling of such high average power levels is inconvenient due to increasingly demanding safety precautionary measures. Thus, SPIFI-CARS would benefit from the employment of lasers with lower repetition rates (\geq readout rate of the detector) reducing the average power while maintaining a sufficient peak power. The scanning process may be accelerated by using faster rotating motors or by employing rotating disks with several sequences of the modulation pattern per full turn or by using an AOD for spatial frequency multiplexing, as already outlined [26].

7. CONCLUSION

SPIFI-CARS links the modulation of the CARS signal in time to the spatial distribution of Raman scatterers. Here, we used two light-sheets (pump and Stokes) of which the Stokes beam was modulated by a rotating amplitude pattern to generate a SPIFI-CARS signal along a line. Using a single element detector, a 1D field of view of $100 \mu\text{m}$ (FWHM) was obtained with up to 40 distinguishable lateral positions (foci). We demonstrated the acquisition of intrinsic confocal SPIFI-CARS and SPIFI-SHG images of polystyrene beads and human breast tissue sections. To evaluate the SNR performance of SPIFI-CARS versus LSM-CARS, we derived a full vectorial model for the computation of SPIFI-CARS 1D profiles. The addition of photon-number-dependent (Poisson noise) and -independent (additive Gaussian) noise contributions revealed the SPIFI-CARS superior performance in the case of sparse samples and for the presence of additive Gaussian noise. Further improvement in the specificity and image acquisition speed above the presented setup includes the implementation of alternative intensity modulation schemes such as AODs, low repetition rate ps-laser sources, as well as the application of fast multi-element detectors, such as PMT arrays.

Funding. Institut National des Sciences de l'Univers, Centre National de la Recherche Scientifique (ANR-11-IDEX-0001-02); Aix-Marseille University A*Midex (A-M-AAP-ID-17-13-170228-15.22-RIGNEAULT); ANR grants France Bio Imaging (ANR-10-INSB-04-01); France Life Imaging infrastructure networks (ANR-11-INSB-0006); Plan Cancer INSERM (18CP128-00, PC201508); National Institutes of Health (R21EB025389, R21MH117786).

Acknowledgment. The content is solely the responsibility of the authors and does not necessarily represent the official views of the National Institutes of Health.

Disclosures. The authors declare no conflicts of interest.

REFERENCES

1. M. T. Cicerone and C. H. Camp, "Histological coherent Raman imaging: a prognostic review," *Analyst* **143**, 33–59 (2018).
2. W. Min, C. W. Freudiger, S. Lu, and X. S. Xie, "Coherent nonlinear optical imaging: beyond fluorescence microscopy," *Annu. Rev. Phys. Chem.* **62**, 507–530 (2011).
3. J.-X. Cheng and X. S. Xie, eds., *Coherent Raman Scattering Microscopy*, Series in Cellular and Clinical Imaging (CRC press, 2016).
4. M. Baumgartl, M. Chemnitz, C. Jauregui, T. Meyer, B. Dietzek, J. Popp, J. Limpert, and A. Tünnermann, "All-fiber laser source for CARS microscopy based on fiber optical parametric frequency conversion," *Opt. Express* **20**, 4484–4493 (2012).
5. T. Gottschall, T. Meyer, M. Baumgartl, C. Jauregui, M. Schmitt, J. Popp, J. Limpert, and A. Tünnermann, "Fiber-based light sources for biomedical applications of coherent anti-Stokes Raman scattering microscopy," *Laser Photon. Rev.* **9**, 435–451 (2015).
6. C. W. Freudiger, W. Yang, G. R. Holtom, N. Peyghambarian, X. S. Xie, and K. Q. Kieu, "Stimulated Raman scattering microscopy with a robust fibre laser source," *Nat. Photonics* **8**, 153–159 (2014).
7. M. D. Duncan, J. Reintjes, and T. J. Manuccia, "Scanning coherent anti-Stokes Raman microscope," *Opt. Lett.* **7**, 350–352 (1982).
8. A. Zumbusch, G. R. Holtom, and X. S. Xie, "Three-dimensional vibrational imaging by coherent anti-Stokes Raman scattering," *Phys. Rev. Lett.* **82**, 4142–4145 (1999).
9. T. Minamikawa, M. Hashimoto, K. Fujita, S. Kawata, and T. Araki, "Multi-focus excitation coherent anti-Stokes Raman scattering (CARS) microscopy and its applications for real-time imaging," *Opt. Express* **17**, 9526 (2009).
10. F. B. Legesse, T. Meyer, S. Heuke, T. Gottschall, T. Pascher, J. Limpert, A. Tünnermann, M. Schmitt, and J. Popp, "Dual-focus coherent anti-Stokes Raman scattering microscopy using a compact two-beam fiber laser source," *Opt. Lett.* **42**, 183 (2017).
11. C. Heinrich, S. Bernet, and M. Ritsch-Marte, "Wide-field coherent anti-Stokes Raman scattering microscopy," *Appl. Phys. Lett.* **84**, 816–818 (2004).
12. P. Berto, A. Jesacher, C. Roeder, S. Monneret, H. Rigneault, and M. Ritsch-Marte, "Wide-field vibrational phase imaging in an extremely folded box-CARS geometry," *Opt. Lett.* **38**, 709 (2013).
13. S. Heuke, K. Unger, S. Khadir, K. Belkebir, P. C. Chaumet, H. Rigneault, and A. Sentenac, "Coherent anti-Stokes Raman Fourier ptychography," *Opt. Express* **27**, 23497–23514 (2019).
14. G. Futia, P. Schlup, D. G. Winters, and R. A. Bartels, "Spatially-chirped modulation imaging of absorption and fluorescent objects on single-element optical detector," *Opt. Express* **19**, 1626–1640 (2011).
15. M. D. Young, J. J. Field, R. A. Bartels, and J. Squier, "Spatial frequency modulated imaging (SPIFI) in amplitude with a spatial light modulator," in *Frontiers in Optics* (OSA, 2016).
16. C. Scotté, S. Sivankutty, P. Stockton, R. A. Bartels, and H. Rigneault, "Compressive Raman imaging with spatial frequency modulated illumination," *Opt. Lett.* **44**, 1936–1939 (2019).
17. F. Legesse, O. Chernavskaja, S. Heuke, T. Bocklitz, T. Meyer, J. Popp, and R. Heintzmann, "Seamless stitching of tile scan microscope images," *J. Microsc.* **258**, 223–232 (2015).
18. O. Chernavskaja, S. Guo, T. Meyer, N. Vogler, D. Akimov, S. Heuke, R. Heintzmann, T. Bocklitz, and J. Popp, "Correction of mosaicking artifacts in multimodal images caused by uneven illumination," *J. Chemom.* **31**, e2901 (2017).
19. D. J. Higley, D. G. Winters, G. L. Futia, and R. A. Bartels, "Theory of diffraction effects in spatial frequency-modulated imaging," *J. Opt. Soc. Am. A* **29**, 2579–2590 (2012).
20. P. A. Stockton, J. J. Field, and R. A. Bartels, "Single pixel quantitative phase imaging with spatial frequency projections," *Methods* **136**, 24–34 (2018).
21. J. J. Field, D. G. Winters, and R. A. Bartels, "Plane wave analysis of coherent holographic image reconstruction by phase transfer (CHIRPT)," *J. Opt. Soc. Am. A* **32**, 2156 (2015).
22. J. J. Field, K. A. Wernsing, S. R. Domingue, A. M. A. Motz, K. F. DeLuca, D. H. Levi, J. G. DeLuca, M. D. Young, J. A. Squier, and R. A. Bartels, "Superresolved multiphoton microscopy with spatial frequency-modulated imaging," *Proc. Natl. Acad. Sci. USA* **113**, 6605–6610 (2016).
23. Microsoft, "Image composite editor," 2015, <https://www.microsoft.com/en-us/research/product/computational-photography-applications/image-composite-editor/>.
24. S. Heuke, N. Vogler, T. Meyer, D. Akimov, F. Kluschke, H.-J. Röwert-Huber, J. Lademann, B. Dietzek, and J. Popp, "Multimodal mapping of human skin," *Br. J. Dermatol.* **169**, 794–803 (2013).
25. S. S. Howard, A. Straub, N. G. Horton, D. Kobat, and C. Xu, "Frequency-multiplexed in vivo multiphoton phosphorescence lifetime microscopy," *Nat. Photonics* **7**, 33–37 (2013).
26. E. D. Diebold, B. W. Buckley, D. R. Gossett, and B. Jalali, "Digitally synthesized beat frequency multiplexing for sub-millisecond fluorescence microscopy," *Nat. Photonics* **7**, 806–810 (2013).
27. C. J. R. Sheppard, "Cylindrical lenses—focusing and imaging: a review [invited]," *Appl. Opt.* **52**, 538–545 (2013).
28. S. Khadir, P. C. Chaumet, G. Baffou, and A. Sentenac, "Quantitative model of the image of a radiating dipole through a microscope," *J. Opt. Soc. Am. A* **36**, 478–484 (2019).
29. J.-X. Cheng, A. Volkmer, and X. S. Xie, "Theoretical and experimental characterization of coherent anti-Stokes Raman scattering microscopy," *J. Opt. Soc. Am. B* **19**, 1363 (2002).
30. E. Gershgoren, R. A. Bartels, J. T. Fourkas, R. Tobey, M. M. Murnane, and H. C. Kapteyn, "Simplified setup for high-resolution spectroscopy that uses ultrashort pulses," *Opt. Lett.* **28**, 361–363 (2003).
31. T. Hellerer, A. M. Enejder, and A. Zumbusch, "Spectral focusing: high spectral resolution spectroscopy with broad-bandwidth laser pulses," *Appl. Phys. Lett.* **85**, 25–27 (2004).